A poly-region boundary element method for two-dimensional Boussinesq flows

G.F. Dargush *, M.M. Grigoriev

*Department of Civil Engineering, State University of New York at Buffalo, Ketter Hall, Box 604300,
Rm 212, Buffalo 142600-4300, NY, USA*

Abstract

A sparse boundary element method (BEM) for steady non-uniformly heated viscous fluid flow is presented. The new boundary integral formulation with a poly-region approach involves the use of region-based convective velocity along with free-space fundamental solutions with slight compressibility in order to eliminate pressure from the governing equations. The boundary element formulation developed previously by the authors for incompressible isothermal viscous fluid flows is extended for non-isothermal flows governed by Boussinesq equations. The new BEM is then applied to the problem of natural convection in a square enclosure, to the classical Rayleigh–Benard problem and to a stratified flow over a backward-facing step. In all three cases, the boundary element results are in good agreement with published finite difference and finite element solutions. However, in some instances, the boundary element solutions are more accurate, particularly in terms of resolving surface tractions and heat flux. Consequently, results are presented in detail to provide data for future comparison. © 2000 Elsevier Science S.A. All rights reserved.

Keywords: Boussinesq equations; Thermal flow; Boundary element method; Natural convection; Rayleigh–Benard problem; Stratified flow

1. Introduction

The problems of thermoviscous flows governed by the Boussinesq equations are of prime importance for many physical processes. Since the 1970s, these problems including natural convection in enclosures, stability analysis in crystal growth, as well as forced convection in heat exchangers, have been successfully solved using finite difference methods (FDM) and finite element methods (FEM). Nowadays, the best commercial computational fluid dynamics (CFD) and computational heat transfer (CHT) codes are based upon the most sophisticated FEM techniques. Although boundary element methods (BEM) that evolved in the early 1980s have advanced greatly, nevertheless, the effectiveness of even the best BEM codes for CFD and CHT is far below that of the commercial FEM codes. There are two primary reasons for the relatively poor performance of BEM. First, traditional BEM formulations lead to full or nearly full system matrices that present a far greater computational burden in comparison with FDM and FEM approaches. Second, standard BEM techniques become numerically unstable at high Reynolds or Rayleigh numbers. The main reason for this latter behavior is due to the use of Stokes flow kernels that are insensitive to the flow direction. The numerical techniques [2,7,23,34] based upon these kernels are quite accurate for low and medium Reynolds numbers, however, these methods fail to converge for highly convective flows. Both finite difference and FEMs also involve numerical instabilities, for

---

* Corresponding author.

example, when the local mesh-based Peclet (or, Reynolds) number is greater than 2. Several stabilized techniques have been proposed [3,18,19] to avoid these difficulties, but all introduce additional numerical error, called numerical diffusivity. For FEMs, recent attempts to reduce the numerical error are made by introducing bubble functions [1,11,12], which provide upwinding (i.e., stabilizing) since the weight functions are sensitive to the convective velocity. Hughes [20,21] showed that the bubble functions lead to approximate element Green's functions in the subgrid scale model, although typically not to a good approximation.

As far as the decoupled model of convective transport is concerned, the convective diffusion fundamental solution that allows recasting the linear partial differential equation into a linear boundary integral equation can be considered an ideal Green's function. Unfortunately, it is not clear how this could be incorporated in FEMs. On the other hand, BEMs based upon this fundamental solution are readily developed and lead to absolutely stable numerical techniques (e.g., [14,17,22,26,29–33]). However, in order to develop a highly accurate BEM, integration must be performed accurately.

Although the BEMs for solving the convective transport equations have been quite successful, the development of BEM for coupled fluid-thermal problems governed by Boussinesq equations remains of major importance. Of course, the model equations for the coupled problem are no longer linear.

Turning to the momentum equation, it appears that the most promising Green's functions for future development of stabilized FEM techniques are the convective Oseen fundamental solutions. Moreover, these convective kernels obtained by Oseen for a linearized flow [27] are ideally suited to the integral formulations for problems of highly convective media. Initial attempts to utilize the so-called Oseenlets for solving the Navier–Stokes equations for small Reynolds number were made by Bush [4] and Lee and Leal [24]. More recently, Dargush et al. [8] and Grigoriev and Fafurin [15] extended the applicability of the boundary integral formulation to higher Reynolds numbers. Then, Grigoriev and Dargush [16] introduced a poly-region BEM for isothermal viscous fluid flows and obtained excellent results for highly convective flows associated with several benchmark problems.

In this paper the authors extend the BEM utilized earlier to non-isothermal flows governed by Boussinesq equations. Details of the new integral formulation and numerical implementation are presented in Sections 2 and 3, respectively. Afterwards, three applications are considered in Section 4. First, the numerical method is applied to natural convection in a square cavity for which a benchmark solution by De Vahl Davis [10] is available. Next, the Rayleigh–Benard problem is comprehensively studied. The critical Rayleigh number at which the onset to convective cells occurs is investigated and favourably compared to the theoretical value obtained by Chandrasekhar [5] using linear stability analysis. Also, numerical results up to $Ra = 10,000$ are compared with the data published by Dakshina Murty [6]. Finally, a stratified flow over a backward-facing step, one of the problems from the Open Boundary Condition Minisymposium, is numerically investigated. Notice that this problem, apart from the previous two, involves both natural and forced convection. The boundary element solution is compared with the benchmark solution obtained by Leone Jr. [25] via bilinear finite elements. For all three problems, the poly-region BEM solutions are presented in both graphical and tabular form to provide data for future comparisons. Included are results for surface traction and heat flux, which are expected to be quite accurate within the present formulation.

2. Governing equations and integral formulation

Consider the steady-state laminar motion of a viscous fluid under the presence of the buoyancy forces due to temperature variations. In this paper we restrict our consideration to the Boussinesq approximation, i.e. the effect of thermal expansion is limited to a linear buoyancy force. Also, the fluid properties such as density ρ, kinematic viscosity v, and thermal diffusivity κ are assumed to be constant parameters, and viscous dissipation of energy is assumed to be negligible. Under these assumptions, the governing set of Navier–Stokes equations is given by:

$$\frac{\partial u_i}{\partial x_i} = 0, \tag{1}$$

$$u_j \frac{\partial u_i}{\partial x_j} = -\frac{1}{\rho} \cdot \frac{\partial P}{\partial x_i} + v \cdot \frac{\partial}{\partial x_j} \left(\frac{\partial u_i}{\partial x_j} + \frac{\partial u_j}{\partial x_i} \right) + \delta_{2i} g \beta_T (T - T_c), \tag{2}$$

$$u_j \frac{\partial T}{\partial x_j} = \kappa \cdot \frac{\partial^2 T}{\partial x_j \partial x_j}, \tag{3}$$

where x_i is the Cartesian co-ordinate with the x_2 axis chosen as vertical, u_i the flow velocity, $P = p + \rho g x_2$ the modified pressure, p the pressure, g the gravitational acceleration, β_T the coefficient of thermal volume expansion, T the temperature, and δ_{ij} is the Kronecker delta. In the momentum Eq. (2) and thereafter, T_c and T_h stand for the reference temperatures of the cooled and heated walls, respectively, and will define a driving buoyancy force.

We introduce the reference quantities for length, velocity, pressure and temperature as given in Table 1, and recast Eqs. (1)–(3) in the following generalized form:

$$\frac{\partial \tilde{u}_i}{\partial \tilde{x}_i} = 0, \tag{4}$$

$$\tilde{u}_j \frac{\partial \tilde{u}_i}{\partial \tilde{x}_j} = -\frac{\partial}{\partial \tilde{x}_i} \tilde{P} + \Lambda \frac{\partial}{\partial \tilde{x}_j} \left(\frac{\partial \tilde{u}_i}{\partial \tilde{x}_j} + \frac{\partial \tilde{u}_j}{\partial \tilde{x}_i} \right) + \delta_{2i} \Phi \tilde{T}, \tag{5}$$

$$\tilde{u}_j \frac{\partial}{\partial \tilde{x}_j} \tilde{T} = \alpha \frac{\partial^2}{\partial \tilde{x}_j \partial \tilde{x}_j} \tilde{T}. \tag{6}$$

Note that Eqs. (4)–(6) are valid for all three problems considered in this paper, namely, (a) natural convection in a square enclosure, (b) a Rayleigh–Benard problem, and, (c) a stratified flow over a backward-facing step, provided that the proper parameters Λ, Φ and α are specified. In Table 1,

$$Fr = \frac{U_m^2}{\beta_T g (T_h - T_c) H}, \quad Pr = \frac{v}{\kappa}, \quad Pe = \frac{U_m H}{\kappa}, \quad Ra = \frac{\beta_T g L^3 (T_h - T_c)}{\kappa v} \quad \text{and} \quad Re = \frac{U_m H}{v}$$

are the Froude, Prandtl, Peclet, Rayleigh and Reynolds numbers, respectively. Here, L is the size of the square cavity for problem (a), L (or H) is the height of the channel for problems (b) and (c), U_m is the mean inlet velocity for the problem (c). From this point onward, we shall omit the tilde for the dimensionless variables for the sake of brevity. Notice that the momentum Eq. (5) and heat transfer Eq. (6) are coupled due to presence of buoyancy forces in the momentum equations, and consequently, need to be considered simultaneously.

In addition to the set of continuity, momentum and heat transfer Eqs. (4)–(6), respectively, governing the behaviour of non-isothermal flow in the domain Ω, the boundary conditions must be specified on the bounding surface Γ. For a general purpose boundary element formulation, velocities $\hat{u}_i$, tractions $\hat{t}_i$, temperatures $\hat{T}$, heat fluxes $\hat{q}_i$ or their combinations, e.g. open boundary conditions, may be specified.

Table 1
Parameters used in Boussinesq equations

Problem	Parameter						
	$\tilde{x}_i$	$\tilde{u}_i$	$\tilde{P}$	$\tilde{T}$	Λ	Φ	α
Natural convection in an enclosure	x_i/L	$u_i L/\kappa$	$PL^2/\rho\kappa^2$	$T - T_c/T_h - T_c$	Pr	$Pr \cdot Ra$	1
Rayleigh–Benard problem	x_i/L	$u_i L/\kappa$	$PL^2/\rho\kappa^2$	$T - T_c/T_h - T_c$	Pr	$Pr \cdot Ra$	1
Stratified flow over a backward-facing step	x_i/H	u_i/U_m	$P/\rho U_m^2$	$T - T_c/T_h - T_c$	$1/Re$	$1/Fr$	$1/Pe$

In order to derive the integral representation of the problem, let us subdivide the domain Ω bounded by surface Γ into a set of N non-overlapping poly-regions Ω_n with the boundaries Γ_n, where $n = 1, 2, \ldots, N$. Next, we decompose the total velocity u_i into the sum

$$u_i^{(n)} = V_i^{(n)} + v_i^{(n)} \tag{7}$$

for each region Ω_n and consider the specific constant velocity $V_i^{(n)}$ as the volume averaged velocity

$$V_i^{(n)} = \frac{\int_{\Omega_n} u_i \, \mathrm{d}\Omega}{\int_{\Omega_n} \mathrm{d}\Omega}. \tag{8}$$

In this case, the integral of the variable part of the total velocity $v_i^{(n)}$ over Ω_n is equal to zero

$$\int_{\Omega_n} v_i \, \mathrm{d}\Omega = 0.$$

Following the approach outlined in the earlier paper [16], first we consider the momentum equation and employ the penalty function formulation

$$p = -\lambda \frac{\partial u_i}{\partial x_i} \tag{9}$$

to eliminate the pressure. Notice that in order to satisfy the continuity equation (4), the penalty parameter should be chosen large enough so that

$$\lambda \gg \Lambda.$$

Now we shall restrict our consideration to the region Ω_n and hence we omit index n for the sake of brevity.
Taking into account (7) and (9) and using free-space convective fundamental solutions

$$
\begin{aligned}
u_{ik}^*(V, y) \\
= \frac{1}{4\pi\Lambda} & \left[\delta_{ik} \exp\left(-\frac{y_j V_j}{2\Lambda} \right) K_0\left(\frac{rV}{2\Lambda} \right) + \frac{1}{rV} (V_i y_k + V_k y_i - \delta_{ik} V_j y_j) \left\{ \frac{2\Lambda}{rV} - \exp\left(-\frac{y_j V_j}{2\Lambda} \right) K_1\left(\frac{rV}{2\Lambda} \right) \right\} \right] \\
- \frac{1}{4\pi\mu} & \left[-\delta_{ik} \exp\left(-\frac{y_j V_j}{2\mu} \right) K_0\left(\frac{rV}{2\mu} \right) + \frac{1}{rV} (V_i y_k + V_k y_i - \delta_{ik} V_j y_j) \left\{ \frac{2\mu}{rV} - \exp\left(-\frac{y_j V_j}{2\mu} \right) K_1\left(\frac{rV}{2\mu} \right) \right\} \right]
\end{aligned}
\tag{10}
$$

based upon region-averaged velocity $V_i^{(n)}$, we can recast the momentum equation (5) into a boundary integral equation

$$
\begin{aligned}
c_{ik}(\xi) u_i(\xi) &+ \int_{\Gamma_n} u_i(x) t_{ik}^*(V, y) \, \mathrm{d}\Gamma(x) + \int_{\Gamma_n} u_i(x) V_j n_j u_{ik}^*(V, y) \, \mathrm{d}\Gamma(x) \\
&= \int_{\Gamma_n} t_i(x) u_{ik}^*(V, y) \, \mathrm{d}\Gamma(x) - \int_{\Omega_n} v_j(x) \frac{\partial u_i}{\partial x_j} u_{ik}^*(V, y) \, \mathrm{d}\Omega(x) + \Phi \int_{\Omega_n} T(x) u_{2k}^*(V, y) \, \mathrm{d}\Omega(x).
\end{aligned}
\tag{11}
$$

Here, n_i is the unit outward normal to the surface Γ_n. In (11), the traction vector

$$t_i = \sigma_{ij} n_j$$

is evaluated from rate-of-deformation

$$\varepsilon_{ij} = \frac{1}{2}\left(\frac{\partial u_i}{\partial x_j} + \frac{\partial u_j}{\partial x_i} \right)$$

and stress tensors

$$\sigma_{ij} = 2\Lambda \varepsilon_{ij} + \lambda \varepsilon_{mm} \delta_{ij}$$

Note that the fundamental solution $u_{ik}^*(V, y)$ satisfies the equation

$$V_j^{(n)} \frac{\partial}{\partial x_j} u_{ik}^* + \frac{\partial}{\partial x_j} \sigma_{ijk}^* + \delta_{ik} \delta(y) = 0. \tag{12}$$

In (10)–(12), the following notations are used

$$\sigma_{ijk}^* = 2\Lambda \varepsilon_{ijk}^* + \lambda \varepsilon_{mmk}^* \delta_{ij},$$

$$\varepsilon_{ijk}^* = \frac{1}{2} \left(\frac{\partial}{\partial x_j} u_{ik}^* + \frac{\partial}{\partial x_i} u_{jk}^* \right),$$

$$t_{ik}^*(V, y) = \sigma_{ijk}^*(V, y) n_j,$$

$$\mu = \lambda + 2\Lambda,$$

$$y_i = x_i - \xi_i,$$

$$r^2 = y_i y_i,$$

$$V^2 = V_i V_i.$$

Also, $\delta(y)$ is the generalized Dirac delta function, $K_0(\cdot)$ and $K_1(\cdot)$ are the modified Bessel functions of the second kind of zeroth- and first-order, respectively.

Notice that the buoyancy force enters the boundary integral equation (11) through the second volume integral. Otherwise the formulation for the momentum equation is identical to that presented in [16].

Next, we consider the linear heat transfer equation with a variable coefficient u_i, representing the local velocity. The integral representation of Eq. (6) may then be written as follows

$$c(\xi)T(\xi) + \int_{\Gamma_n} q(x)T^*(V, y)\,\mathrm{d}\Gamma(x) + \int_{\Gamma_n} T(x)V_j n_j T^*(V, y)\,\mathrm{d}\Gamma(x)$$

$$= \int_{\Gamma_n} T(x)q^*(V, y)\,\mathrm{d}\Gamma(x) + \int_{\Omega_n} v_j(x)\frac{\partial T}{\partial x_j} T^*(V, y)\,\mathrm{d}\Omega. \tag{13}$$

Here

$$T^*(V, y) = \frac{1}{4\pi\alpha} \exp\left(-\frac{y_j V_j}{2\alpha} \right) K_0\left(\frac{rV}{2\alpha} \right) \tag{14}$$

is the free-space fundamental solution to the linear convective diffusion equation

$$V_j \frac{\partial}{\partial x_j} T^*(V, y) + \alpha \frac{\partial^2}{\partial x_j \partial x_j} T^*(V, y) + \delta(y) = 0. \tag{15}$$

Notice that for uniform velocity fields, the volume integral in (13) vanishes, so that transfer phenomena will be expressed solely in terms of boundary values.

In (13),

$$q = -\alpha \frac{\partial T}{\partial n}$$

is the diffusive heat flux along the normal direction to the boundary Γ and in (14)

$$q^*(V, y) = -\alpha \frac{\partial}{\partial n} T^* = \frac{1}{4\pi\alpha} \exp\left(-\frac{y_j V_j}{2\alpha} \right) \left[V_k n_k K_0\left(\frac{rV}{2\alpha} \right) + \frac{Vy_k n_k}{r} K_1\left(\frac{rV}{2\alpha} \right) \right] \tag{16}$$

is the flux associated with the kernel $T^*(V, y)$. We would prefer to deal with the diffusive heat flux q in the integral equation (13), rather than with the total heat flux due to both diffusion and convection

$$q_T = -\alpha \frac{\partial T}{\partial n} + u_i n_i T$$

as the latter quantity is usually not specified for open boundaries.

3. Numerical implementation

3.1. Introduction

In order to numerically solve the set of integral equations (11) and (13), we follow the numerical approximation developed in the earlier paper [16]. We subdivide the domain of interest Ω into hexagonal volume regions and utilize octagonal volume regions only where hexagonal regions are not suitable. Note that these poly-regions prevent the overdeterminancy of the global matrix. In this section, we will concentrate only on those aspects of the numerical implementation that differ from those outlined by Grigoriev and Fafurin [15] and Grigoriev and Dargush [16].

3.2. Spatial discretization and integration

Similar to Grigoriev and Dargush [16], we consider a twelve-noded hexagonal region (or, a 16-noded octagonal region as a transition region) for the geometric representation of the region Ω_n, as illustrated in Fig. 1. Each region is then subdivided into 3 (or 4 for octagons) eight-noded quadratic quadrilateral cells in order to numerically evaluate the volume integrals in (11) and (13). Notice that in addition to the region

□ region internal node (u_1, u_2, T)
○ mid-node (u_1, u_2, t_1, t_2, T, q)
● vertex node (u_1, u_2, s_{11}, s_{12}, s_{21}, s_{22}, T, q_1, q_2)

(a)

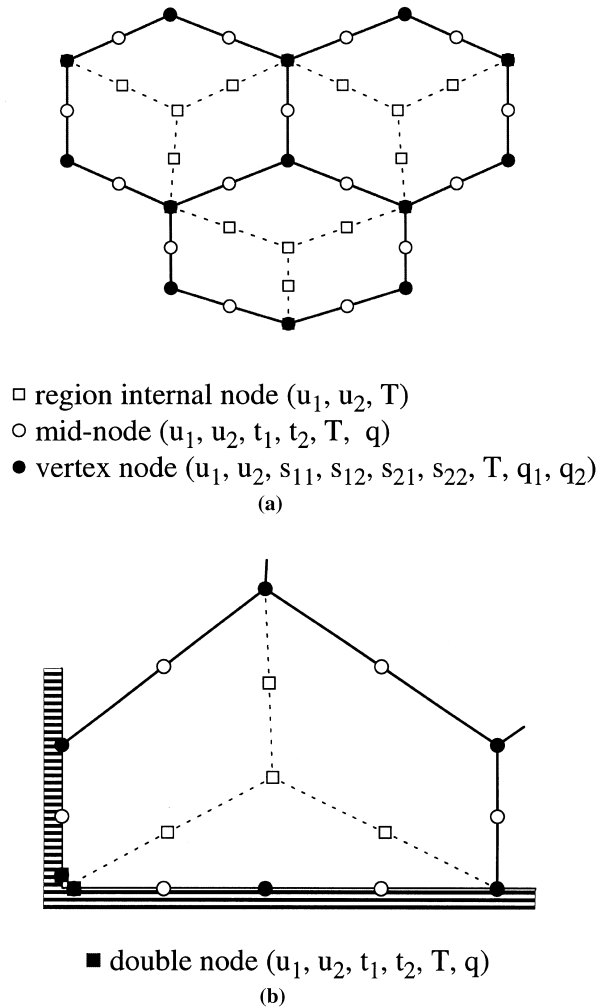■ double node (u_1, u_2, t_1, t_2, T, q)

(b)

Fig. 1. Hexagonal regions and collocation nodes: (a) internal regions; (b) boundary region with a double node.

boundary nodes we introduce 4 (or 5 for octagons) internal nodes to permit the subdivision of the regions into eight-noded volume cells.

Considering quadratic shape functions $N_\alpha(\eta)$ to approximate velocities u_i, temperatures T, tractions t_i and heat fluxes q along the quadratic boundary elements and biquadratic shape functions $M_\alpha(\eta_1, \eta_2)$ to represent velocities and temperatures for the eight-noded cells, we discretize integral equations (11) and (13) for each poly-region Ω_n as follows:

$$
\begin{aligned}
c_{ik}u_i + &\sum_{l=1} u_{il}^{(\alpha)} \int_{\Gamma_l} N_\alpha(\eta) t_{ik}^*(V, y)\, \mathrm{d}\Gamma(x) + \sum_{l=1} u_{il}^{(\alpha)} V_j n_j \int_{\Gamma_l} N_\alpha(\eta) u_{ik}^*(V, y)\, \mathrm{d}\Gamma(x) \\
&= \sum_{l=1} t_{il}^{(\alpha)} \int_{\Gamma_l} N_\alpha(\eta) u_{ik}^*(V, y)\, \mathrm{d}\Gamma(x) - \sum_{e=1} u_i^{(\alpha)} \int_{\Omega_e} v_j \frac{\partial}{\partial x_j} M_\alpha(\eta_1, \eta_2) u_{ik}^*(V, y)\, \mathrm{d}\Omega(x) \\
&\quad + \Lambda \sum_{e=1} T^{(\alpha)} \int_{\Omega_e} M_\alpha(\eta_1, \eta_2) u_{2k}^*(V, y)\, \mathrm{d}\Omega(x),
\end{aligned}
\tag{17}
$$

$$
\begin{aligned}
cT + &\sum_{l=1} q_l^{(\alpha)} \int_{\Gamma_l} N_\alpha(\eta) T^*(V, y)\, \mathrm{d}\Gamma(x) + \sum_{l=1} T_l^{(\alpha)} V_j n_j \int_{\Gamma_l} N_\alpha(\eta) T^*(V, y)\, \mathrm{d}\Gamma(x) \\
&= \sum_{l=1} T_l^{(\alpha)} \int_{\Gamma_l} N_\alpha(\eta) q^*(V, y)\, \mathrm{d}\Gamma(x) + \sum_{e=1} T^{(\alpha)} \int_{\Omega_e} v_j \frac{\partial}{\partial x_j} M_\alpha(\eta_1, \eta_2) T^*(V, y)\, \mathrm{d}\Omega(x),
\end{aligned}
\tag{18}
$$

respectively. In (17) and (18), Γ_l represents the lth boundary element and Ω_e stands for the eth eight-noded volume cell of the poly-region Ω_n.

As noted by Grigoriev and Dargush [16], the overall accuracy of the boundary element formulation utilizing convective kernels mainly depends upon the accuracy of the numerical integrations over boundary elements and volume cells. In this paper, the semi-analytical approach outlined by Grigoriev and Fafurin [15] is used to evaluate integrals over the boundary elements. Note that integration of the kernel t_{ik}^* over a boundary element in (17) involves a strong $1/\eta$-type singularity. Therefore, these strongly singular integrals, existing only in the Cauchy principal value sense, are evaluated indirectly in the way outlined earlier [15,16].

In the integral equation (18), integration of the kernel $q^*(V, y)$ also involves a strong $1/\eta$-type singularity when the source point lies on the boundary element. However, since

$$
y_i n_i = 0
$$

for the singular boundary element, expression (18) simplifies to the form

$$
q^*(V, y) = \frac{V_k n_k}{2} T^*(V, y).
\tag{19}
$$

Therefore, the integral involving $q^*(V, y)$ in (18) is no longer strongly singular.

To accurately evaluate the volume integrals in (17) and (18) that involve weakly singular kernels, non-uniform subsegmentation of the volume cells is used. The volume integral involving buoyancy forces in (17) requires higher order accuracy compared to the other volume integrals since it represents the driving force rather than merely residual forces.

The overall accuracy of the BEM mainly depends upon the accuracy of the boundary and volume integrations. Consequently, we recommend checking the results of those integrations by using the exact solution for fully developed stratified viscous flow between two parallel horizontal plates (i.e. stratified Poiseuille flow) with the following conditions:

$$
u_i = 0 \text{ and } T_{\mathrm{c}} = 0 \text{ at } x_2 = 0 \text{ together with } u_i = 0 \text{ and } T_{\mathrm{h}} = 1 \text{ at } x_2 = H.
\tag{20}
$$

The velocity, pressure and temperature fields satisfying Eqs. (4)–(6) and boundary conditions (20) are given by:

$$u_1(x_2) = \frac{4x_2}{H}\left(1 - \frac{x_2}{H}\right),$$

$$u_2 = 0,$$

$$p(x_1, x_2) = \frac{1}{2 \cdot H \cdot Fr} x_2^2 - \frac{8v}{H^2} x_1,$$

$$T(x_2) = \frac{x_2}{H}.$$

(21)

We emphasize that since the distribution of any variable for this specified flow is at most quadratic and we utilized quadratic and biquadratic shape function, the residual in integral equations (17) and (18) due to flow field (21) will indicate the level of accuracy for both boundary and volume integration. Other simplified buoyancy driven flows allowing an exact solution provide us with a cubic velocity distribution (e.g., consider fully developed natural convection between two parallel vertical infinite plates), and hence are useful only with cubic and bicubic shape functions.

3.3. Assembly

Since the governing Boussinesq equations are coupled (i.e., momentum equations include temperature and the heat transfer equation involves the velocity field), we will assemble nodal variables associated with both velocity and temperature fields into one global matrix and then solve the resulting equations simultaneously. Following the earlier work [16], we write integral equations (17) and (18) for each collocation node (Fig. 1a). For every boundary mid-node we formulate six (four for Eq. (17) and two for (18)) linearly independent discrete integral equations; exactly three equations for each of the neighbouring regions. The degrees of freedom for the mid-node is also reduced to six (two components of the velocity vector, two components of the traction vector, one temperature and a diffusive heat flux) after compatibility conditions between neighbouring regions I and II are applied:

$$u_i^{(\mathrm{I})} = u_i^{(\mathrm{II})}, \quad t_i^{(\mathrm{I})} = -t_i^{(\mathrm{II})}, \quad T^{(\mathrm{I})} = T^{(\mathrm{II})}, \quad q^{(\mathrm{I})} = -q^{(\mathrm{II})}.$$

For every region vertex node we may write nine (six for Eq. (17) and three for (18)) independent equations; exactly three equations for each of three neighbouring regions. This number is equal to the degrees of freedom for the region vertex node, since we consider four components of the stress tensor and two components of the heat flux vector in addition to two components of the velocity vector and temperature.

The region internal nodes were introduced to subdivide the poly-regions into eight-noded volume cells. Consequently, we need to consider only three degrees of freedom for each internal node; namely, two components of the velocity vector and temperature. Moreover, these degrees of freedom associated with the region internal nodes are eliminated from the global set of equations at the assembly stage, similar to the procedure described in the earlier paper [16].

A well-posed elliptic problem requires that exactly three degrees of freedom be specified at each global domain Ω boundary collocation node (i.e., two for the momentum equation and one for the heat transfer equation). Notice that each boundary vertex node neighbours with two regions, so that exactly six linearly independent equations may be written. Recalling that each vertex node involves nine field components with three specified as boundary conditions, we shall have only six degrees of freedom which is equal to the number of linearly independent equations at these nodes. Similarly, we find that the degrees of freedom for the boundary mid-node is three and that we also may write three linearly independent equations at each of these nodes. The domain corners are handled as double nodes (see Fig. 1b) which greatly improves the numerical solution at the corner regions. Notice that each of the double nodes introduces three degrees of freedom, similar to a boundary mid-node.

Having considered all types of collocation nodes, we have now demonstrated that the global set of equations is not overdetermined. After the region-by-region assembly is completed, we arrive at the global set of non-linear equations

$$\underset{\sim}{A}(\underset{\sim}{x})\underset{\sim}{x} = \underset{\sim}{b}.$$

(22)

Here, the global vector $\underset{\sim}{x}$ contains a mixture of generalized velocities, stresses, tractions, temperatures and diffusive heat fluxes. As the global matrix $A(x)$ depends on the local region-based convective velocity V_i and, in general, is directly related to the nodal velocities u, we linearize (22) with an assumption that $\underset{\sim}{V}$ does not change during an iteration step. Then, the set of linearized equations

$$A(\underset{\sim}{x}^{(q-1)})\underset{\sim}{x}^{(q)} = \underset{\sim}{b} \tag{23}$$

is solved at every iteration q using the direct method for a sparse set of equations presented by Østerby and Zlatev [28]. In some cases, the efficiency of the numerical method may be greatly increased by considering the global matrix $A(\underset{\sim}{x}^{(q)})$ to be constant during several iterations so that the most time-consuming operation is eliminated.

4. Numerical results

4.1. Introduction

A C++ code for the steady-state viscous fluid flow developed in the previous work [16] has been modified to implement the numerical method outlined in Sections 2 and 3. Although the numerical code has been applied to non-isothermal viscous flows within rather simple geometries, it has been developed to also model flows in complex geometries. Note that the code has the capability to both couple and decouple the momentum and heat transfer equations. The decoupled problem, of course, produces two smaller global matrices. Numerical experiments showed that convergence characteristics for the coupled approach are higher than for the decoupled, though perhaps not as high as might be expected.

As a numerical exercise, we consider the stratified Poiseuille flow that possesses quadratic distribution of the longitudinal velocity, linear distribution of the temperature and at most quadratic distribution of the pressure. The boundary conditions on the lower and upper walls are given by (20), the inlet velocity and temperature distributions are specified as (21), while outflow (open) boundary conditions are utilized as follows:

$$\frac{\partial T}{\partial n} = 0 \quad \text{and} \quad t_1 = P.$$

The unknown outflow pressure distribution is re-evaluated at each iteration using the outflow temperature profile assuming that the flow is fully developed when it leaves the computational domain.

The numerical experiments have been run on a series of hexagonal meshes and demonstrated the high accuracy of the numerical solutions. Specifically, the nodal-based numerical errors for the velocity, temperature and pressure are only slightly higher than the error emerging when directly checking the accuracy of the coefficients via stratified Poiseuille flow as described in Section 3.2, and may be attributed to the imposed open boundary conditions as well as double node corner error. The maximum nodal-based numerical errors are less than 0.005%, 0.0003%, and 0.01% for velocity, temperature and outflow pressure, respectively, for the rather fine mesh of 217 hexagonal regions for $Fr = 1$.

In the remainder of this work we consider three test problems: (a) natural convection in a square cavity, (b) the Rayleigh–Benard problem with the solid-solid boundaries, and (c) stratified flow over a backward-facing step. Note that for problems (a) and (c) there are benchmark numerical solutions available to test the accuracy of the BEM presented here. Surprisingly, for the Rayleigh–Benard problem, no benchmark solutions are available. The best numerical solution is obtained by Dakshina Murty [6], however, Chandrasekhar [5] presented a linear stability analysis for the problem.

4.2. Natural convection in a square enclosure

Contrary to driven cavity flow, the problem of natural convection in a square enclosure involves no singularity for velocity and temperature fields, although tractions and heat fluxes are discontinuous at the corners. This is one reason that natural convection in a square enclosure is useful as a benchmark problem to test CFD codes, even though it requires consideration of the temperature field. Instead of the

mathematically well-posed problem of natural convection in a cavity, most CFD developers use the ill-posed driven cavity problem to justify their CFD codes.

The problem under consideration has been intensively studied by many investigators, and De Vahl Davis and Jones [9] summarized numerical results obtained by different authors using different methods. The benchmark solutions obtained by De Vahl Davis [10] on a series of rather moderate finite difference grids using Richardson extrapolation were utilized to check the accuracy of the numerical methods. Since then, although De Vahl Davis' benchmark solutions have been challenged many times by a variety of numerical studies, these solutions proved to be quite accurate.

The purpose here is to obtain numerical results as accurately as possible using the proposed BEM and then to compare these results with the benchmark solutions of De Vahl Davis [10]. The problem domain and specified boundary conditions are shown in Fig. 2. Note that no-slip boundary conditions are specified on all boundaries, and upper and lower walls are thermally insulated. In this paper, we consider natural convection for Rayleigh numbers as high as $Ra = 10^6$. The numerical solutions are obtained on the non-uniform boundary element mesh shown in Fig. 3, which consists of 612 hexagonal regions. To show that this mesh is sufficient to obtain mesh-independent results, we carried out a convergence study for $Ra = 10^5$. As seen from Table 2, very good results are obtained even on a rather coarse mesh.

Numerical solutions for all Rayleigh numbers are obtained starting from the state when fluid is at rest. Convergence is assumed to occur for a relative tolerance 10^{-5} with respect to the root-mean-square of the velocity field. A penalty parameter $\lambda = 10^{10}$ is used throughout the paper.

We should emphasize that convergence is very fast for lower Rayleigh numbers and then becomes slow as the Rayleigh number increases. For example, only six iterations were needed for $Ra = 10^3$, whereas slightly above 300 iterations along with under-relaxation were required to obtain a convergence for $Ra = 10^6$. Such a slow convergence for higher Rayleigh number flows is due to the fact that for some regions (i.e., at the vicinity of the vertical walls) the buoyancy forces are in equilibrium with the pressure gradient, while the convective and diffusive terms are negligibly small. Therefore, the convective kernels utilized for the momentum equation are no longer suitable. In order to improve the convergence characteristics, further development of the present BEM should employ modified kernels that directly incorporate the buoyancy forces.

The numerical results for the natural convection in a square cavity are presented for four different Rayleigh numbers, namely, $10^3, 10^4, 10^5$ and 10^6, and are compared to the benchmark solutions provided by De Vahl Davis [10]. Figs. 4–6 illustrate the streamline, temperature and pressure contours, respectively, for
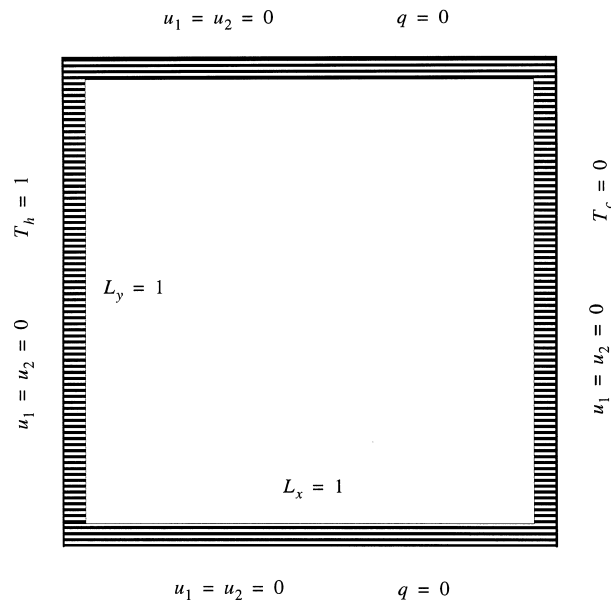

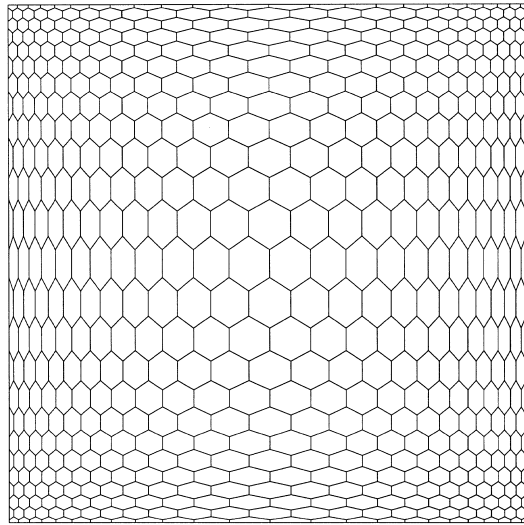Fig. 2. Problem statement for natural convection in a square enclosure.

Fig. 3. Boundary element mesh for the problem of a natural convection in a square enclosure.

Table 2
Natural convection in a square enclosure $Ra = 10^5$, $Pr = 0.71$, convergence study

BEM mesh	ψ_{mid}	First extremum $\psi_{\min}$ at (x_1, x_2)	Second extremum $\psi_{\min}$ at (x_1, x_2)	$\overline{Nu}$	$\overline{\tau}_{\mathrm{w}}$ at $x_2 = 0$	$\overline{\tau}_{\mathrm{w}}$ at $x_1 = 0$
8 × 8 76 hexagonal regions	−9.113	−9.629 (0.281, 0.602)	−9.626 (0.717, 0.398)	4.520	−412.2	1180.0
12 × 12 162 hexagonal regions	−9.109	−9.612 (0.283, 0.602)	−9.616 (0.716, 0.398)	4.522	−411.9	1180.3
18 × 18 351 hexagonal regions	−9.114	−9.615 (0.285, 0.601)	−9.614 (0.715, 0.399)	4.521	−412.1	1180.4
24 × 24 612 hexagonal regions	−9.114	−9.615 (0.285, 0.601)	−9.615 (0.715, 0.399)	4.522	−412.1	1180.4
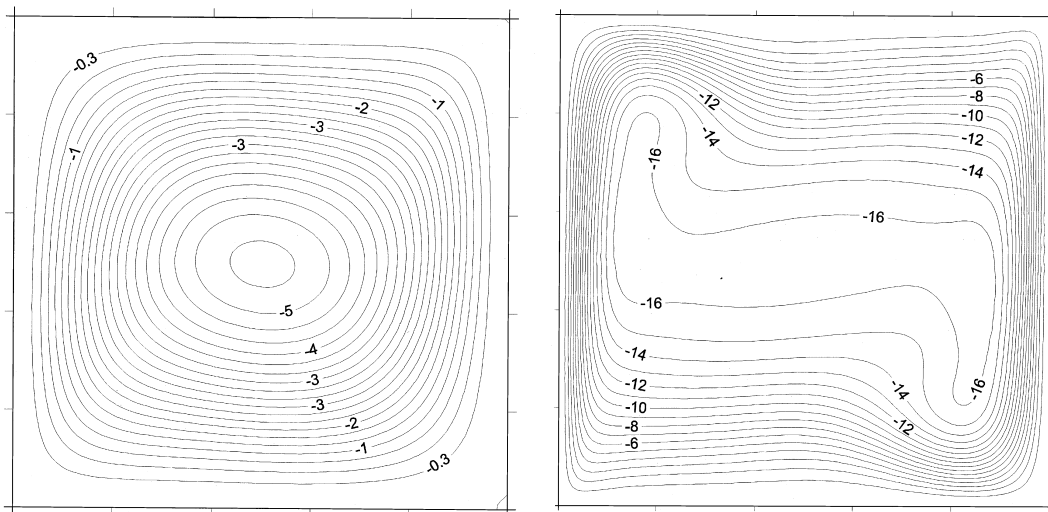
Fig. 4. Natural convection in a square encosure: (a) streamline contours for $Ra = 10^4$; (b) streamline contours for $Ra = 10^6$.
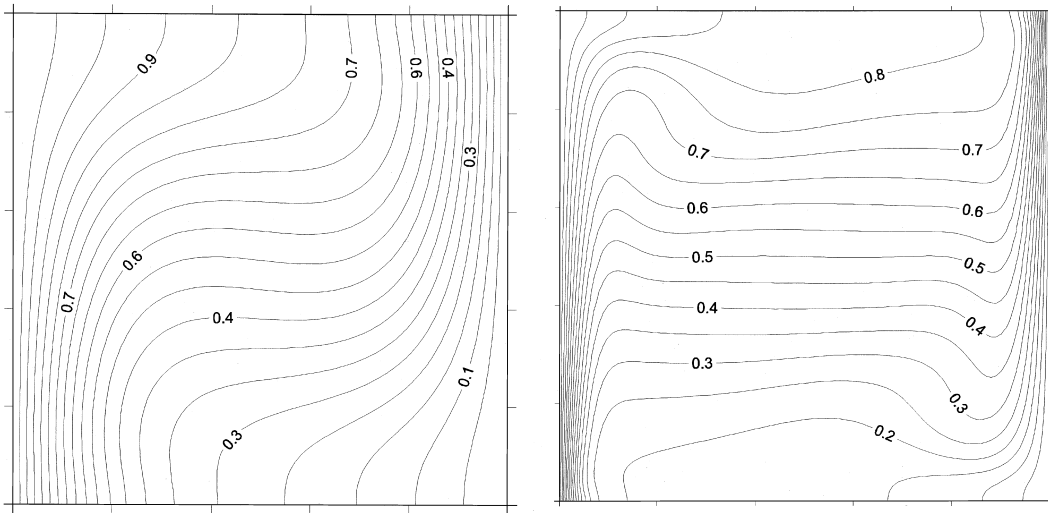
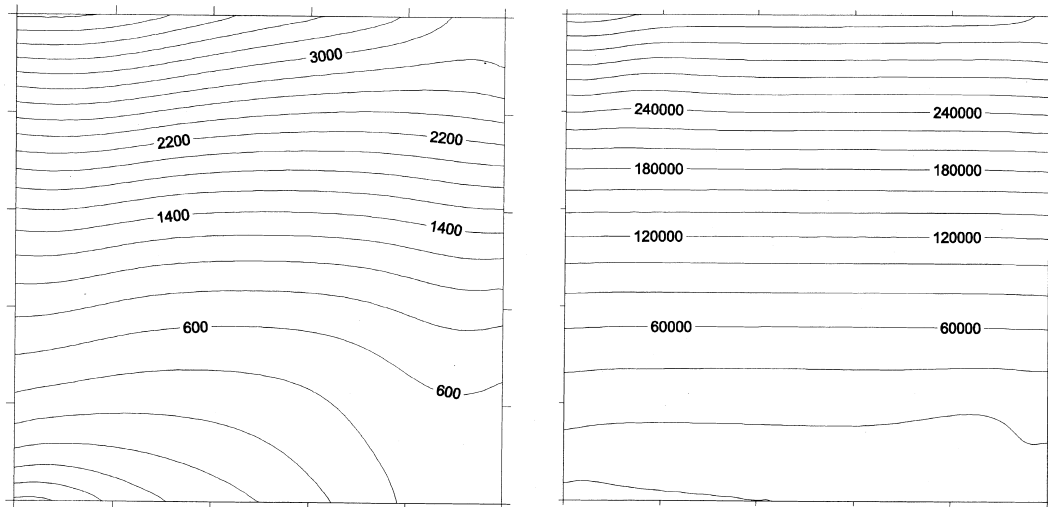Fig. 5. (a) Temperature contours for $Ra = 10^4$. (b) Temperature contours for $Ra = 10^6$.

Fig. 6. (a) Pressure contours for $Ra = 10^4$. (b) Pressure contours for $Ra = 10^6$.

the problem at $Ra = 10^4$ and $Ra = 10^6$. Note that all contours are plotted with uniform increments. We present the tabulated data for only the highest Rayleigh number, $Ra = 10^6$. Velocity and temperature profiles along the vertical and horizontal centerlines are presented in Tables 3 and 4, respectively.

The horizontal velocity u_1 on the vertical centerline (Fig. 7a) and the vertical velocity u_2 on the horizontal centerline (Fig. 7b) are presented for all Rayleigh numbers. As we see from Fig. 7b, as well as from the contour plots presented in Figs. 4 and 5, the circulation within the vast central region is very weak. However, in the vicinity of the vertical walls, the boundary layer is formed which is thinner than the thermal boundary layer (see Fig. 8), since the Prandtl number $Pr = 0.71$ is less than 1. A proper resolution close to vertical walls is mandatory to obtain a good numerical solution.

Fig. 9 represents the distributions of wall shear stresses on all four walls of the cavity for different Rayleigh numbers. Notice that flow in a square cavity is symmetric about a center of the cavity. The distribution of the wall shear stresses (Fig. 9) together with the distribution of the Nusselt number over the walls (Fig. 10) clearly exemplifies this phenomena.

Table 3
Natural convection in a square enclosure (velocity and temperature profiles at $x_1 = 0.5$ for selected nodal points. $Ra = 10^6$ and $Pr = 0.71$)

x_2	u_1	u_2	T
0	0	0	0.1671
0.01818	−13.42	−0.153	0.1671
0.04616	−31.43	−0.422	0.1681
0.08933	−52.95	0.446	0.1735
0.14277	−64.87	2.738	0.1893
0.19548	−59.65	2.928	0.2160
0.25774	−42.54	0.308	0.2648
0.33249	−22.45	−1.642	0.3396
0.37516	−14.17	−1.456	0.3827
0.42234	−7.709	−0.946	0.4283
0.5	−0.585	−0.415	0.5002
0.57766	7.354	0.762	0.5714
0.66750	24.11	2.792	0.6590
0.74225	44.41	1.482	0.7350
0.78972	56.97	−0.767	0.7738
0.84471	64.19	−1.555	0.8049
0.87988	60.52	−0.523	0.8181
0.92025	47.14	0.805	0.8277
0.95384	30.07	0.891	0.8322
0.97517	17.17	0.433	0.8336
1	0	0	0.8349

Table 4
Natural convection in a square enclosure (velocity and temperature profiles at $x_2 = 0.5$ for selected nodal points. $Ra = 10^6$ and $Pr = 0.71$)

x_1	u_1	u_2	T
0	0	0	1
0.01804	1.502	169.55	0.8496
0.05043	3.174	206.41	0.6207
0.08912	−1.543	96.08	0.4908
0.13744	−4.796	11.08	0.4778
0.19516	−1.523	−5.94	0.4975
0.24104	1.079	−2.37	0.5022
0.29346	1.880	0.62	0.5008
0.35335	1.216	0.87	0.4991
0.42179	0.177	0.01	0.4988
0.5	−0.585	−0.41	0.5002
0.57820	−1.047	−0.51	0.5014
0.64664	−1.538	−0.80	0.5014
0.70653	−1.852	−0.39	0.4997
0.75896	−0.940	2.53	0.4985
0.80483	1.695	6.12	0.5027
0.86255	4.956	−10.49	0.5025
0.91087	1.670	−95.71	0.5096
0.94956	−3.085	−206.17	0.3794
0.98195	−1.487	−169.44	0.1502
1	0	0	0

For the sake of future comparisons with other CFD and CHT codes, we provide tabulated boundary data for the highest Rayleigh number considered in this paper, $Ra = 10^6$. Table 5 presents the wall shear stresses and Nusselt numbers along the both vertical walls for the selected points. Additional data will be provided to researchers upon request.
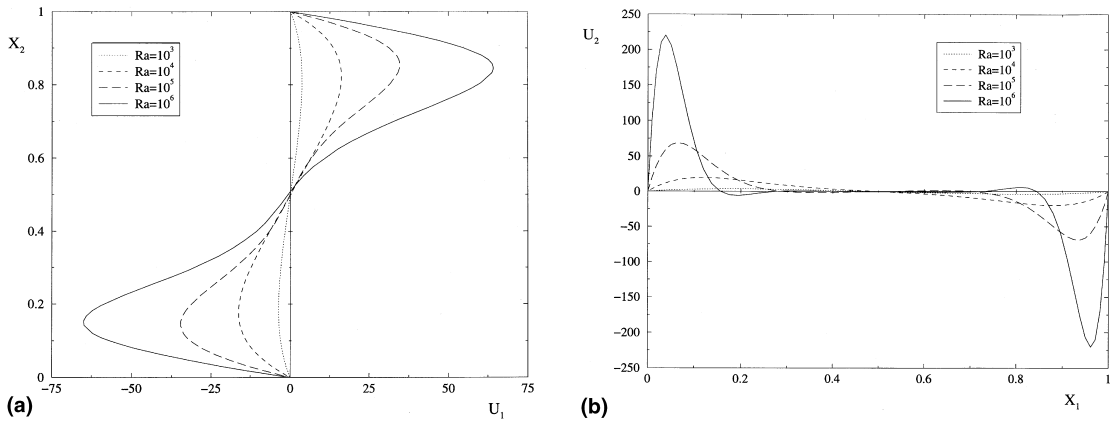
Fig. 7. (a) Horizontal velocity profiles along the vertical centerline. (b) Vertical velocity profiles along the horizontal centerline.
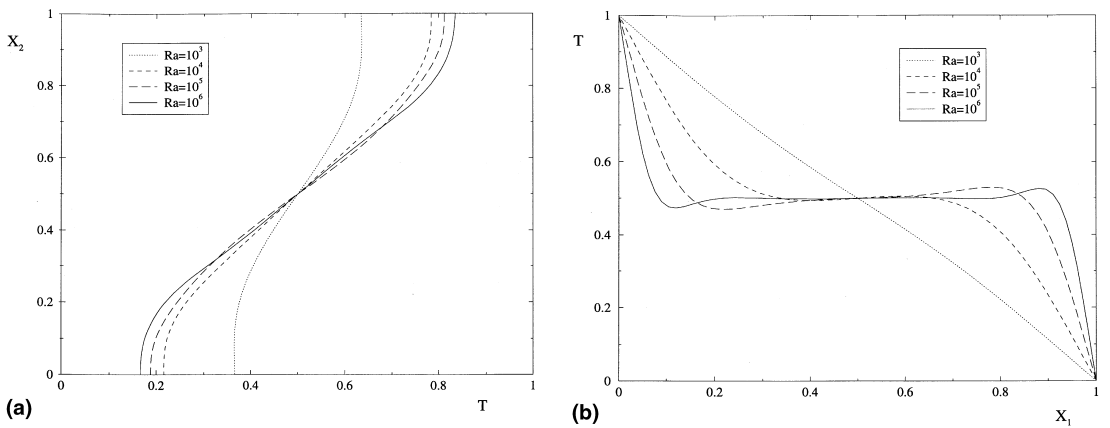
Fig. 8. (a) Temperature profiles along the vertical centerline. (b) Temperature profiles along the horizontal centerline.
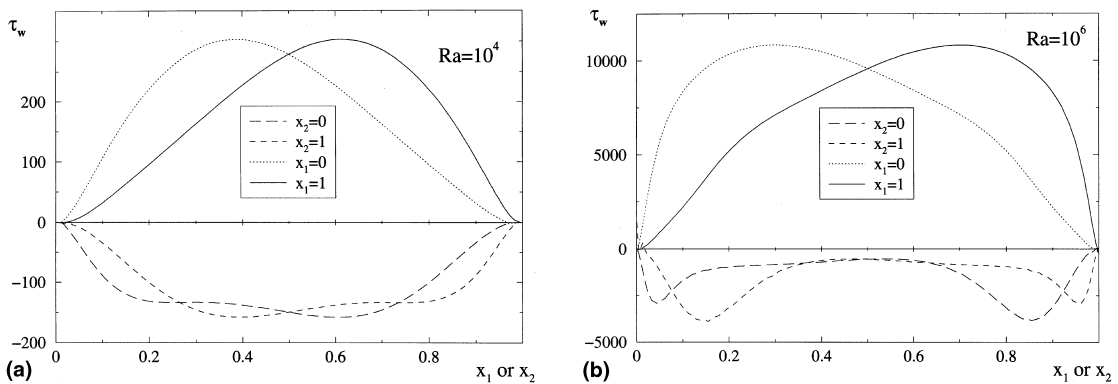
Fig. 9. Wall shear stresses in a square enclosure.

Finally, for the problem of natural convection in a square cavity, we summarize the numerical results in Table 6, where the BEM solutions are compared with the benchmark solutions of De Vahl Davis [10]. Although the agreement is excellent, we assume that the BEM solutions are more accurate than that of De Vahl Davis [10], as no extrapolation is involved in this work.
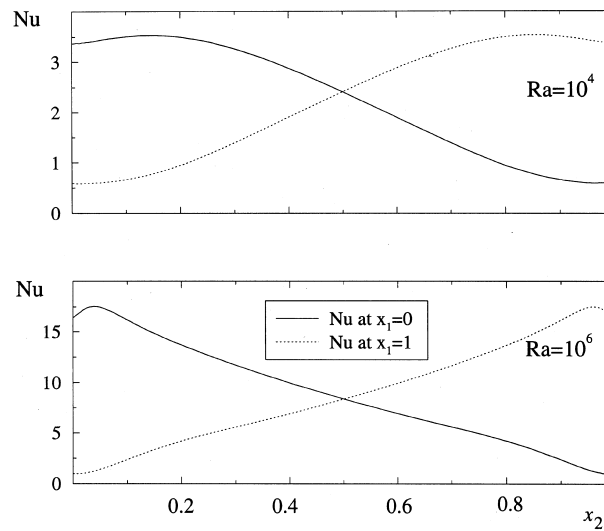
Fig. 10. Nusselt number along the vertical wall for a problem of natural convection in a cavity.

Table 5
Natural convection in a square enclosure (distributions of wall shear stresses and Nusselt numbers along the vertical walls, $Ra = 10^6$ and $Pr = 0.71$)

x_2	$x_1 = 0$		$x_1 = 1$	
	τ_w	Nu	τ_w	Nu
0.01003	800.4	16.801	32.0	0.988
0.02718	3148.5	17.427	317.5	1.088
0.05175	5805.7	17.445	925.3	1.419
0.07415	7244.5	16.941	1495.1	1.850
0.10622	8548.4	16.021	2393.4	2.511
0.15529	9713.9	14.715	3907.1	3.454
0.19643	10,306.6	13.771	5107.1	4.154
0.25774	10,752.7	12.520	6453.1	5.043
0.32003	10,817.2	11.362	7394.3	5.851
0.40769	10,426.4	9.856	8499.8	7.017
0.5	9600.2	8.393	9570.7	8.366
0.59230	8533.0	7.045	10,400.3	9.831
0.67996	7427.1	5.879	10,797.9	11.337
0.74225	6485.0	5.070	10,738.1	12.495
0.80356	5134.1	4.179	10,295.1	13.745
0.84470	3928.4	3.476	9703.0	14.690
0.89377	2406.5	2.528	8538.1	15.994
0.92585	1504.1	1.863	7235.3	16.916
0.94824	932.0	1.431	5798.2	17.418
0.97281	315.1	1.097	3142.4	17.395
0.98996	41.9	0.997	799.4	16.770

4.3. Rayleigh–Benard problem

Next we consider the classical Rayleigh–Benard problem. Fluid resides between two infinite horizontal plates and is uniformly heated from below. When the temperature gradient, i.e. Rayleigh number, is low, the fluid is stable and remains motionless. Starting from some critical Rayleigh number, Ra_{cr}, the fluid is no longer motionless and breaks up into Benard cells. Chandrasekhar [5], based upon the theory of linear stability, showed that $Ra_{cr} = 1708$ for this case of solid–solid boundaries.

Table 6
Natural convection in a square enclosure (comparison with the benchmark solutions of De Vahl Davis)

Property	$Ra = 10^3$		$Ra = 10^4$		$Ra = 10^5$		$Ra = 10^6$	
	BEM	de Vahl Davis	BEM	de Vahl Davis	BEM	de Vahl Davis	BEM	de Vahl Davis
ψ_{mid}	−1.175	−1.174	−5.074	−5.071	−9.114	−9.111	−16.37	−16.32
First extremum ψ_{min}	–	–	–	–	−9.615	−9.612	−16.83	−16.750
at x_1, x_2					0.285, 0.601	0.285, 0.601	0.151, 0.546	0.151, 0.547
Second extremum ψ_{min}					−9.615	–	−16.77	–
at x_1, x_2	–	–	–	–	0.715, 0.399		0.850, 0.451	
u_{1max}	3.650	3.649	16.18	16.18	34.72	34.73	64.19	64.63
at $x_1 = 0.5, x_2$	0.813	0.813	0.823	0.823	0.855	0.855	0.845	0.850
u_{1min}	−3.650	–	−16.18	–	−34.73	–	−65.04	–
at $x_1 = 0.5, x_2$	0.187		0.177		0.145		0.150	
u_{2max}	3.697	3.697	19.63	19.617	68.63	68.59	220.62	219.36
at $x_1, x_2 = 0.5$	0.178	0.178	0.119	0.119	0.066	0.066	0.037	0.0379
u_{2min}	−3.697	–	−19.63	–	−68.61	–	−220.32	–
at $x_1, x_2 = 0.5$	0.822		0.881		0.934		0.962	
T_{max}	0.635	–	0.784	–	0.812		0.835	
at $x_1 = 0.5, x_2$	0.920		0.985		1	–	1	–
T_{min}	0.365	–	0.216	–	0.188		0.167	
at $x_2, x_1 = 0.5$	0.080		0.016		0	–	0	–
$\overline{Nu}$	1.118	1.118	2.245	2.243	4.522	4.519	8.824	8.800
Nu_{max}	1.508	1.505	3.531	3.528	7.719	7.717	17.55	17.925
at x_2	0.069	0.092	0.145	0.143	0.069	0.081	0.0395	0.0378
Nu_{min}	0.694	0.692	0.597	0.586	0.751	0.729	0.980	0.989
at x_2	0.997	1	0.966	1	0.979	1	1	1
$\overline{\tau}_w$ at $x_2 = 0$	−19.44	–	−108.2	–	−412.1	–	−1399	–
$\overline{\tau}_w$ at $x_1 = 0$	20.37	–	171.1	–	1180.4	–	7370	–

Although the physical problem is considered for an infinite domain, we cannot specify boundary conditions at infinity since the problem is periodic. Ideally, all Benard cells forming due to fluid instability could be described with the period L_{cell}. If the period of the cell were known a priori, we could easily restrict our consideration to a simple cell and apply open boundary conditions for both sides of the cell either as

$$u_1 = u_2 = 0 \quad \text{on } x_1 = \pm L_{cell}/2, \tag{24}$$

$$u_1 = t_2 = 0 \quad \text{on } x_1 = \pm L_{cell}/2. \tag{25}$$

These boundary conditions are equivalent, since condition (24) implies $t_2 = 0$ on the periodic boundary as

$$\frac{\partial}{\partial x_1}(\cdot) = 0$$

due to periodicity. And vice versa, if $t_2 = 0$ is specified on the periodic boundary, this does not contradict the result $u_2 = 0$ from continuity Eq. (4). Therefore, we need to consider either boundary condition (24) or (25) to model the Rayleigh–Benard problem. Notice that the normal traction cannot be specified on the open boundaries, because the pressure is not given there. In fact, the pressure depends upon flow pattern.

Unfortunately, the size of the cell L_{cell}, or period, is not known a priori. Instead, it should be obtained numerically as it may depend upon the Rayleigh number once the flow breaks up into cells. To allow numerical simulation, we consider a finite domain of length $L = 11$ and height $H = 1$ and discretize it into a

uniform mesh with 796 hexagonal regions, as shown in Fig. 11. On the lower and upper plates, the no-slip boundary conditions are specified. The lower plate is heated at uniform temperature $T_h = 1$, while the temperature on the upper plate is maintained at zero, $T_c = 0$. On the vertical boundaries of the computational domain, we specified conditions (24) together with $q = 0$, i.e., we introduce vertical thermally
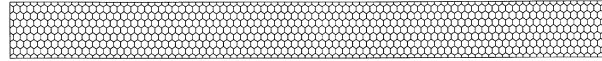

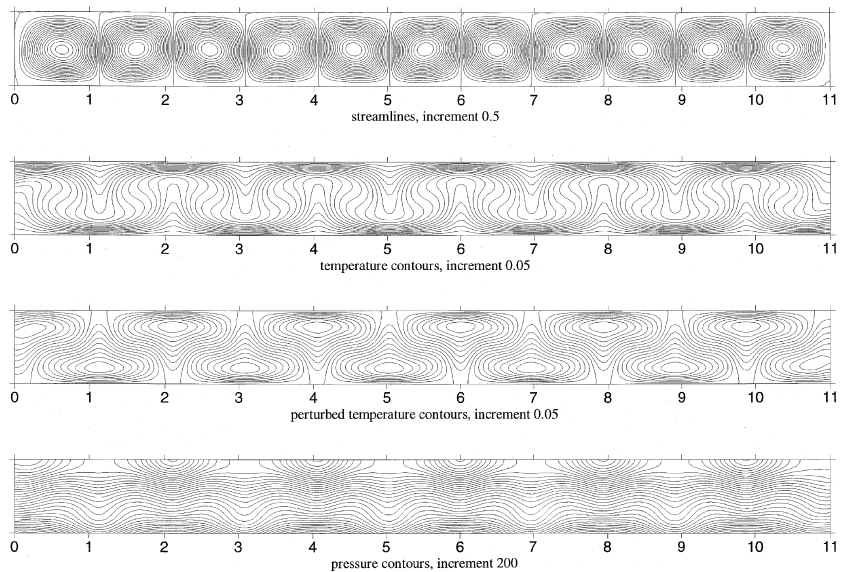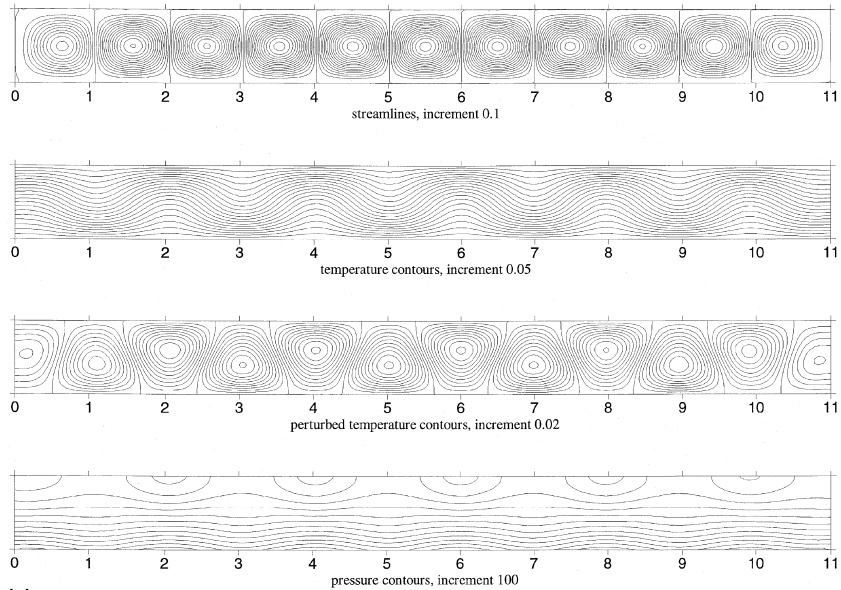Fig. 11. Boundary element mesh for the Rayleigh–Benard problem.

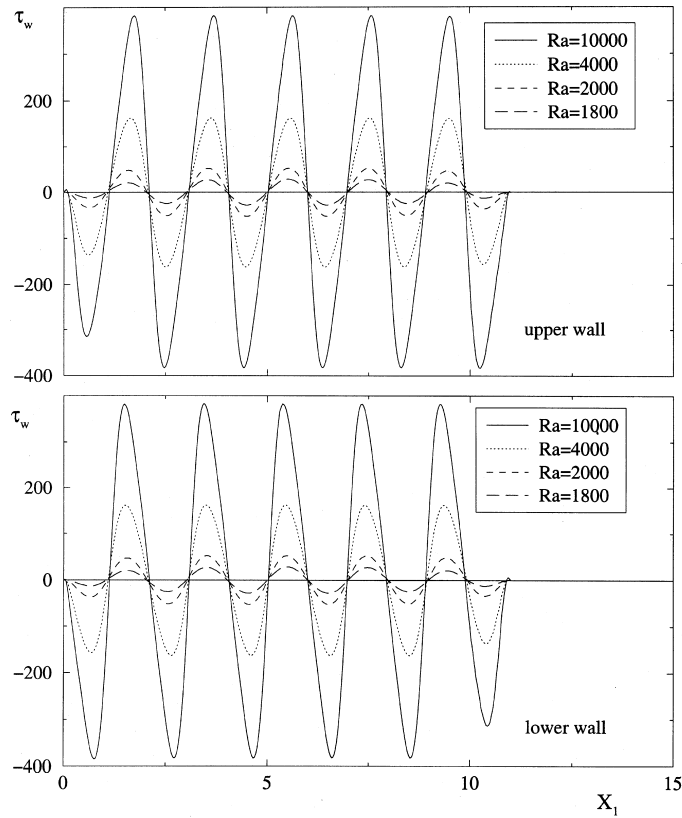Fig. 12. (a) Rayleigh–Benard problem, $Ra = 2000$. (b) Rayleigh–Benard problem, $Ra = 10{,}000$.

Fig. 13. Distributions of wall shear stresses along lower and upper plates for the Rayleigh–Benard problem.

insulated boundaries. Numerical experiments with the boundary conditions (24) and (25) for various Rayleigh numbers showed that the difference between results are negligibly small. All solutions presented in this paper are obtained using condition (24).

We consider numerical solutions for Rayleigh numbers up to 10,000 with the Prandtl number $Pr = 1$. Comparisons are made with the results obtained by Dakshina Murty [6] using FEM. Up to $Ra_{cr} = 1710 \pm 0.5$, the fluid remains at rest and heat transfer is only due to diffusion. The temperature profile is given by

$$T(x_2) = 1 - x_2. \tag{26}$$

When the Rayleigh number is greater than Ra_{cr}, natural convection occurs and the heat transfers due to both diffusion and convection. Notice that convective heat transfer will become dominant as the Rayleigh number increases. The critical Rayleigh number, $Ra_{cr} = 1710 \pm 0.5$, is close to the theoretical value $Ra_{cr} = 1708$ obtained by Chandrasekhar [5] and the numerical value of $Ra_{cr} = 1710$ published by Dakshina Murty [6]. Although the transition to convection cells should occur at some distinct critical Rayleigh number, we specify only an interval for the critical number as it is very difficult to distinguish the transition with a higher level of precision within the context of the steady-state equations. The flow pattern does not change abruptly for the steady-state problem and convergence difficulties were encountered in the range $Ra_{cr} < Ra < 1800$. If more accuracy is desired, stability of the fluid to small perturbations could be precisely analyzed by developing a time-dependent formulation, but this is beyond the present scope.

The streamfunction, temperature, perturbed temperature defined as the deviation of the flow temperature distribution from the motionless linear profile (26) and pressure contours of the flow for $Ra = 2000$ and 10,000 are shown in Fig. 12. In general, the intensity of the cells increases as the Rayleigh number grows. Moreover, the cells become skewed for higher Rayleigh numbers. Although cells close to the vertical walls

differ from the middle cells, at least three cells in the center of the domain possess similar properties for all Rayleigh numbers considered. As the Rayleigh number increases, more cells become symmetric with respect to the vertical inter-cell boundary lines, and interestingly the numerical convergence improves.

The distributions of wall shear stresses (Fig. 13) and local Nusselt numbers (Fig. 14) also demonstrate flow periodicity. Note that points with $\tau_w = 0$ are used to obtain the size of the cell with a high level of accuracy. The numerical data for the Rayleigh–Benard problem is summarized in Table 7. Here we also included data obtained by Dakshina Murty [6] for no-slip boundary conditions on the vertical walls. As is seen from Table 7, the BEM and FEM results agree quite well. Note that here
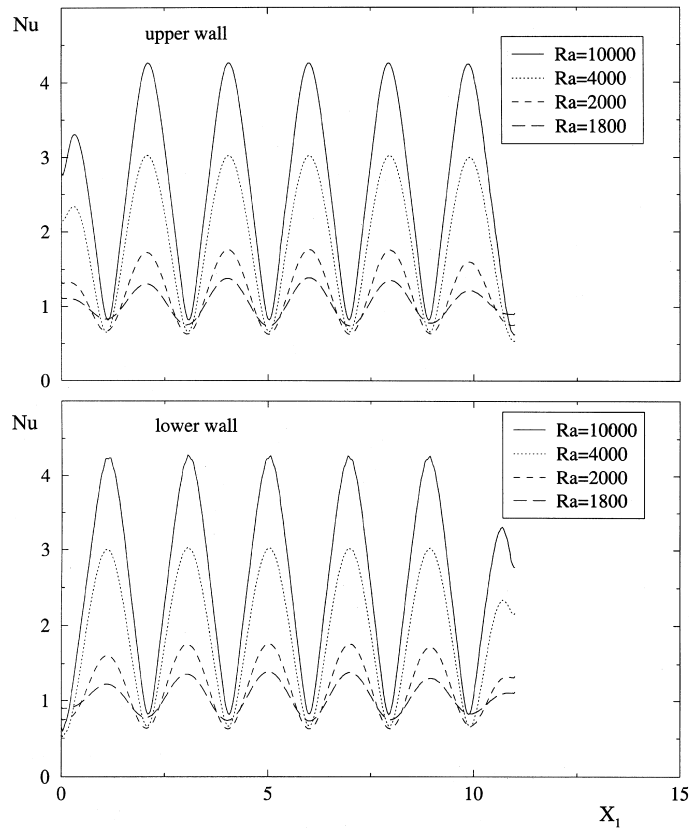

Fig. 14. Distributions of the Nusselt number along the horizontal walls for the Rayleigh–Benard problem.

Table 7
The Rayleigh–Benard problem (average Nusselt number and the mid-cell properties)

Ra	$\overline{Nu}$		Middle cell properties			
	BEM	Dakshina Murty, FEM case I	$\overline{Nu}_{cell}$	ψ_{max}	$\overline{\tau}_w$	L_{cell}
1800	1.048	–	1.069	0.849	17.91	0.994
1900	1.115	–	1.143	1.257	26.65	0.990
2000	1.179	–	1.211	1.555	33.12	0.986
3000	1.627	1.625	1.664	3.336	73.60	0.978
4000	1.890	1.887	1.929	4.512	102.5	0.978
6000	2.217	2.220	2.260	6.309	151.0	0.976
10,000	2.606	2.604	2.656	9.000	235.2	0.972

$$\overline{Nu}_{\text{cell}} = \frac{1}{L_{\text{cell}}} \int_{\tilde{x}_1}^{\tilde{x}_1 + L_{\text{cell}}} Nu(x_1) \, dx_1$$

and

$$\bar{\tau}_{\text{w}} = \frac{1}{L_{\text{cell}}} \int_{\tilde{x}_1}^{\tilde{x}_1 + L_{\text{cell}}} \tau_{\text{w}}(x_1) \, dx_1,$$

where $\tilde{x}_1$ is the position of the left-hand side boundary of the middle cell. As the uniformity of the cells improves, the difference between $\overline{Nu}$ and $\overline{Nu}_{\text{cell}}$ decreases.

Finally, the data tabulated in Table 7 is plotted in Fig. 15. Notice that the size of the Benard cells decreases slightly as the Rayleigh number increases.

4.4. Stratified flow over a backward-facing step

The last problem we consider in this paper is a stratified flow over a backward-facing step with the Reynolds and Peclet numbers of 800, a Froude number of 16/9 and a Prandtl number of 1. This is one of the Open Boundary Condition Symposium test problems. A benchmark solution to the test problem was obtained by Leone Jr. [25] using FEM employing bilinear finite elements for velocity and temperature, and piecewise constant elements for pressure. Notice that Gartling [13] used higher order finite elements to obtain a benchmark solution for isothermal flow over a backward-facing step for a similar
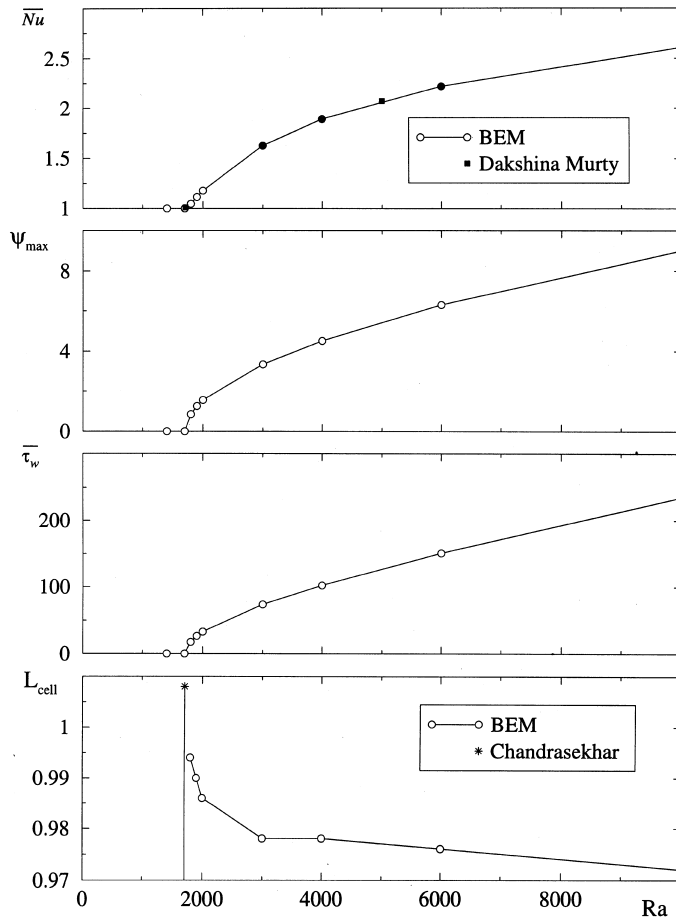

Fig. 15. Averaged Nusselt number and the mid-cell properties for the Rayleigh–Benard problem.

Reynolds number and for approximately the same number of finite elements. Therefore we should anticipate that the numerical solution obtained by Leone Jr. [25] is less accurate than that of Gartling [13].

Similar to the earlier work [16], we again introduce an entrance region before the step, as shown in Fig. 16. This is more physically appropriate than the case when the inflow boundary and expansion coincide. The effect of the inflow boundary location on the isothermal backward-facing step flow was examined in the earlier work [16]. Here the inflow boundary is located 0.02 step heights upstream of the expansion in order to compare numerical results obtained using the BEM with those provided by Leone Jr. [25]. As pointed out by Grigoriev and Dargush [16], the flow over a backward-facing step involves a stress singularity due to the step corner. This singularity is present even when the inflow boundary is located on the expansion.

The boundary conditions specified for the problem are shown in Fig. 16. Notice that for the outflow boundary the normal traction $t_1 = 0$ is no longer valid as was the case for the isothermal flow. The pressure distribution for stratified Poiseuille flow far downstream is given by Eq. (21), however, it is better to re-evaluate pressure after each iteration. Assuming that the flow far downstream is fully developed, we get from the momentum Eq. (5) the following

$$p(x_1, x_2) = \frac{1}{H \cdot Fr} \int_0^{x_2} T(x_1, y)\, \mathrm{d}y + f(x_1) \tag{27}$$

for $x_1 = L$. Since the pressure is arbitrary, we set $f(x_1) = 0$.

Based upon numerical results obtained for the isothermal flow over a backward-facing step using BEM [16], we utilized a similar boundary element mesh of 558 mostly hexagonal regions, as shown in Fig. 17. This level of mesh refinement is sufficient to obtain numerical results with a high level of accuracy.

Fig. 18 shows the normalized difference between calculated velocity, temperature and pressure at the outflow boundary with the analytic solution (21) for the stratified Poiseuille flow. Note that the flow field is quite close to the fully developed distribution. This indicates that the outflow boundary is far enough downstream and that the backward-facing step flow is not significantly influenced by the truncation of the domain.

Fig. 19 illustrates the streamfunction, temperature and pressure contours. Notice that there are present five eddies in the flow: three on the lower wall and two on the upper wall. A similar flow pattern has been
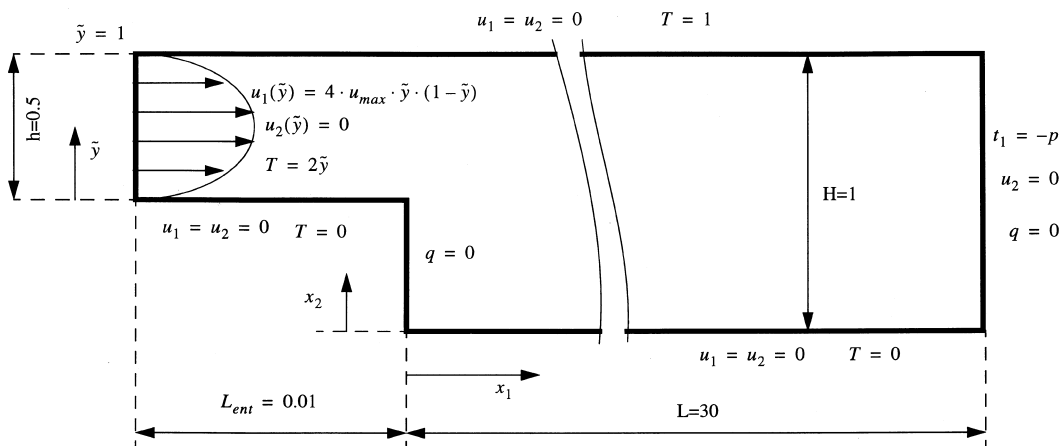

Fig. 16. Computational domain and boundary conditions for the stratified flow over a backward-facing step.

Fig. 17. Boundary element mesh of 558 regions for the backward-facing step flow problem.
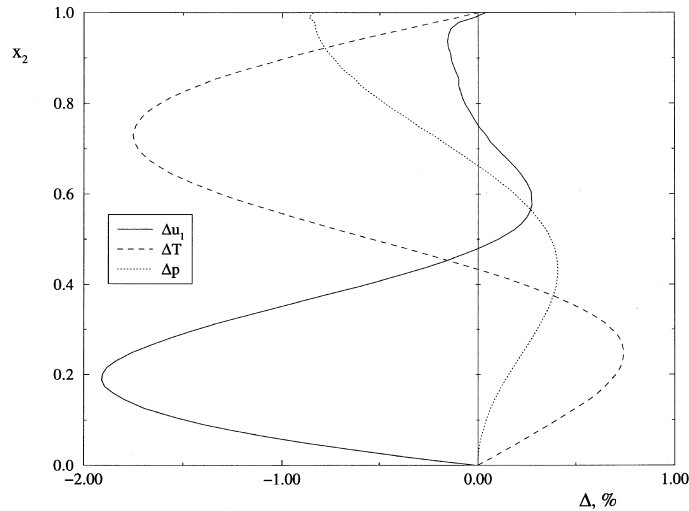
Fig. 18. Difference between the BEM and exact solution for the fully developed stratified flow at the outflow boundary.
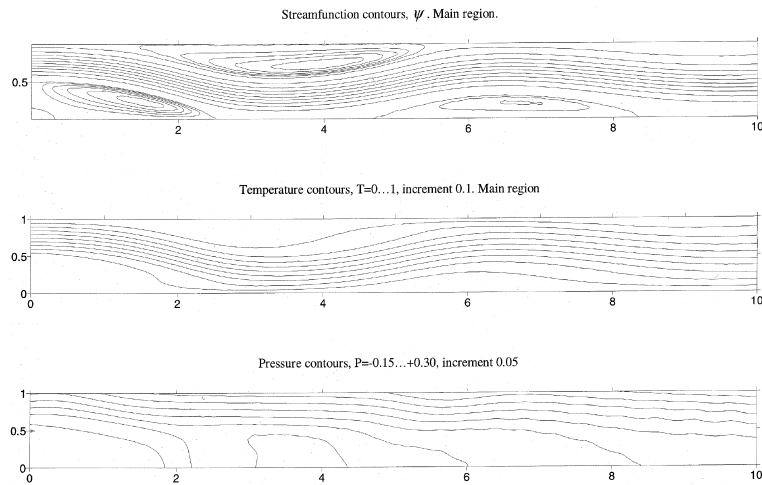

Fig. 19. Stratified flow over a backward facing step, $Re = 800$.

obtained by Leone Jr. [25]. Interestingly, compared to the associated isothermal flow, the number of eddies increases, while the length of the main eddy behind the step reduces significantly.

Next we present tabulated data for the velocity and temperature profiles for three different cross-sections. The data given in Table 8 may be useful in validating CFD and CHT numerical codes. Although plots of this data are similar to those provided by Leone Jr. [25], unfortunately, without tabulated data detailed comparison is hardly possible.

With the present BEM, tractions and heat fluxes are evaluated directly and possess a high level of accuracy. Consequently, the wall shear stresses and Nusselt numbers on both horizontal walls are presented in Table 9 at selected points to allow comparison with other numerical solutions. Notice that the wall shear stresses have not reached the developed value, namely, ± 0.00375, although results are quite close. The distributions of wall shear stresses and pressure along lower and upper walls are also plotted in Fig. 20. Points at which the wall shear stress is zero, $\tau_w = 0$, are used to locate the starting and ending points of the eddies. We should emphasize that the pressure gradient in the vertical direction is much higher as it equilibrates the buoyancy force.

Table 8
Stratified flow over a backward facing step (cross-channel profiles, $Re = 800$)

y	u_1			$u_2 \times 10^2$			T		
	$x_1 = 3$	$x_1 = 7$	$x_1 = 15$	$x_1 = 3$	$x_1 = 7$	$x_1 = 15$	$x_1 = 3$	$x_1 = 7$	$x_1 = 15$
0	0	0	0	0	0	0	0	0	0
0.05	0.3744	−0.0499	0.1109	−0.968	0.040	−0.019	0.1199	0.0291	0.0557
0.1	0.6298	−0.0641	0.2188	−3.068	0.064	−0.069	0.2017	0.0566	0.1110
0.15	0.8705	−0.0424	0.3251	−5.256	−0.054	−0.138	0.2606	0.0803	0.1650
0.2	1.0845	0.0132	0.4308	−7.138	−0.365	−0.203	0.3295	0.1000	0.2170
0.25	1.2348	0.1018	0.5343	−8.469	−0.917	−0.252	0.4088	0.1185	0.2667
0.3	1.2986	0.2229	0.6318	−9.117	−1.693	−0.274	0.4928	0.1411	0.3144
0.35	1.2634	0.3756	0.7171	−8.967	−2.640	−0.2641	0.5778	0.1727	0.3610
0.4	1.1315	0.5522	0.7839	−8.074	−3.671	−0.224	0.6602	0.2152	0.4072
0.45	0.9203	0.7376	0.8263	−6.565	−4.618	−0.160	0.7369	0.2677	0.4535
0.5	0.6689	0.9051	0.8403	−4.815	−5.369	−0.082	0.8035	0.3273	0.4999
0.55	0.4275	1.0331	0.8246	−3.220	−5.828	−0.001	0.8567	0.3918	0.5462
0.6	0.2331	1.1031	0.7808	−2.052	−5.933	0.071	0.8939	0.4589	0.5923
0.65	0.0955	1.1073	0.7133	−1.296	−5.692	0.123	0.9165	0.5268	0.6381
0.7	0.0070	1.0473	0.6282	−0.830	−5.141	0.149	0.9296	0.5932	0.6843
0.75	−0.0441	0.9334	0.5317	−0.548	−4.371	0.149	0.9388	0.6548	0.7319
0.8	−0.0686	0.7817	0.4292	−0.339	−3.489	0.126	0.9481	0.7121	0.7818
0.85	−0.0728	0.6077	0.3241	−0.185	−2.544	0.092	0.9590	0.7717	0.8341
0.9	−0.0611	0.4152	0.2177	−0.075	−1.513	0.053	0.9718	0.8418	0.8884
0.95	−0.0362	0.2033	0.1099	−0.014	−0.496	0.017	0.9857	0.9206	0.9440
1	0	0	0	0	0	0	1	1	1

Table 9
Stratified flow over a backward-facing step (wall shear stresses and Nusselt number along the lower and upper walls)

| x_1	Lower wall, $x_2 = 0$		Upper wall, $x_2 = 1$	
	$\tau_w \times 10^2$	$Nu \times 10^2$	$\tau_w \times 10^2$	$Nu \times 10^2$
0.121	0.0042	0.0096	−1.4313	0.2537
0.342	0.0007	0.0135	−1.1610	0.2298
0.646	−0.0281	0.0234	−0.6853	0.1959
0.998	−0.0801	0.0378	−0.1949	0.1464
1.264	−0.1476	0.0539	0.0347	0.1076
1.557	−0.3064	0.0848	0.1394	0.0701
2.055	−0.7818	0.1898	0.1435	0.0318
2.530	0.0827	0.2941	0.1120	0.0303
3.066	1.3173	0.3096	0.1046	0.0370
3.803	0.7286	0.2223	0.1576	0.0573
4.657	−0.0421	0.1006	0.3655	0.1255
5.648	−0.1224	0.0401	−0.1858	0.2615
6.796	−0.1543	0.0641	−0.5944	0.2187
8.126	−0.1101	0.1482	0.0020	0.1034
9.398	0.3211	0.1871	0.0530	0.0864
10.829	0.2097	0.1444	−0.0732	0.1252
12.456	0.1840	0.1311	−0.2391	0.1445
14.687	0.2741	0.1391	−0.2731	0.1404
16.808	0.3092	0.1391	−0.3088	0.1405
19.219	0.3312	0.1379	−0.3354	0.1404
22.525	0.3477	0.1357	−0.3556	0.1394
25.669	0.3546	0.1334	−0.3627	0.1385
29.242	0.3550	0.1306	−0.3765	0.1400
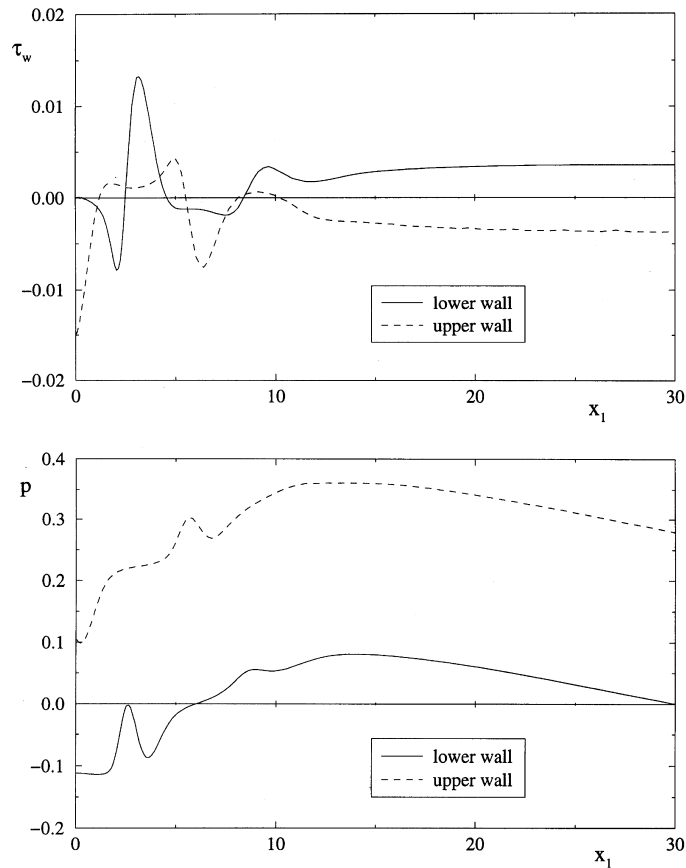
Fig. 20. Distributions of the wall shear stresses and pressure along the horizontal walls for the stratified backward-facing step flow.
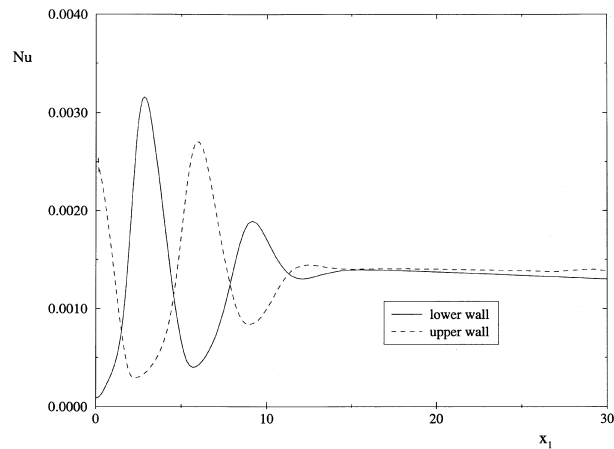

Fig. 21. Nusselt number on the horizontal wall for the problem of the stratified backward-facing step flow.

The Nusselt number on the lower wall reaches it peak value in the region where the flow rebounds from the lower wall, see Fig. 21. Consistently, when the Nusselt number increases on the lower wall, the Nusselt number decreases on the upper wall, and vice versa. Notice that this is due to the flow bouncing from wall to wall. Also, the numerical values of Nusselt number differ significantly from that of the stratified Poiseuille flow, 0.00125, since it takes much longer than 30 step heights, used in the work, in order to get fully developed flow.

Table 10
Eddy positions and their lengths (comparison with the benchmark data of Leone Jr.)

Eddy	Start, x_1		Stop, x_1		Length	
	Leone Jr.	BEM	Leone Jr.	BEM	Leone Jr.	BEM
1 (lower)	0	0	0.355	0.35	0.355	0.35
2 (lower)	0.355	0.35	2.508	2.50	2.153	2.15
3 (lower)	4.565	4.56	8.413	8.42	3.848	3.86
4 (upper)	1.215	1.21	5.512	5.51	4.297	4.30
5 (upper)	8.188	8.12	10.234	10.18	2.046	2.06

Table 11
Eddy streamfunction extremum value and its position (comparison with the benchmark data of Leone Jr.)

Eddy	Extremum value		Leone Jr.		BEM	
	Leone Jr.	BEM	x_1	x_2	x_1	x_2
1 (lower)	0.00008	0.000005	0.0125	0.100	0.06	0.110
2 (lower)	−0.02241	−0.02240	1.500	0.2417	1.57	0.221
3 (lower)	−0.00852	−0.00855	6.625	0.200	6.67	0.205
4 (upper)	0.51880	0.51866	4.042	0.7417	4.00	0.735
5 (upper)	0.50017	0.49984	9.208	0.950	9.13	0.941

Finally, we summarize the numerical results obtained by the BEM in Tables 10 and 11 and compare them with the benchmark solution of Leone Jr. [25]. Although the agreement between the data is quite good, better agreement was obtained with those of Gartling [13] for the isothermal backward-facing step flow studied in the earlier paper [16]. As we mentioned above, the numerical solution of Leone Jr. [25] is expected to be less accurate than that of Gartling [13] since the former investigator utilized lower order finite elements.

5. Conclusion

A new boundary element formulation for non-isothermal viscous fluid flow governed by Boussinesq equations is presented in this paper. The coupled momentum and heat transfer equations are recast to the corresponding integral forms using Oseenlets involving an artificial compressibility and convective diffusion kernels, respectively. The poly-region BEM utilizes a region-based convective velocity formulation to improve convergence characteristics as well as to dramatically reduce the number of fill-ins in the global assembled matrix. This results in a highly accurate, computationally efficient method for Boussinesq flow. A quantitative study of the computational efficiency of the method was reported previously within the context of steady two-dimensional isothermal flow [16]. That study revealed that the new BEM was at least competitive with standard finite element approaches. We expect similar behavior for Boussinesq flows.

The boundary element formulation has been used for three non-isothermal problems governed by Boussinesq equations. First, the natural convection in a square cavity has been studied for Rayleigh numbers up to 10^6 on a very fine mesh. It has been shown that the numerical solutions are in excellent agreement with the benchmark solution obtained by De Vahl Davis [10]. Tabulated results are presented for $Ra = 10^6$ to provide data for general CHT code validation. The authors emphasize that the problem of natural convection in a square cavity is well-posed mathematically, includes many challenges related to flow circulation and, therefore, recommend it as a test problem for all CHT codes. On the other hand, the widely used problems of driven cavity flow and backward-facing step flow involve singularities in the velocity field and stresses, respectively.

Next, the well-known Rayleigh–Benard problem has been comprehensively studied. The numerical results indicate that the transition to the convective mode occurs at $Ra_{cr} = 1710 \pm 0.5$ which is close to the theoretical result obtained by Chandrasekhar [5], $Ra_{cr} = 1708$, and to the numerical result of Dakshina Murty [6], $Ra_{cr} = 1710$, obtained using FEM. The boundary condition issue for the periodic problem has been discussed. Since the size of the Benard cells in the problem is not known a priori, a finite domain including 11 cells are considered in this work. No-slip conditions are applied on the insulated vertical sidelines. It should be emphasized that the authors experienced numerical difficulties due to lack of convergence for the convective flow immediately after the transition to the Benard cells. However, for the flows at $Ra \geqslant 1800$, convergent steady-state solutions exist. We believe there is no steady-state solution for the region $Ra_{cr} < Ra < 1800$.

Finally, we considered the stratified flow over a backward-facing step for which a benchmark numerical solution was obtained by Leone Jr. [25]. Although the BEM and the benchmark [25] solutions are in quite good agreement, we expect that the BEM solution is more accurate than the finite element solution published by Leone Jr. [25]. Also to allow validation of CHT codes, we presented some tabulated data including velocity and temperature profiles at selected cross-sections, as well as distributions of wall shear stresses and Nusselt Numbers.

As a closure we should point out that further BEM developments for non-isothermal fluid flows governed by Boussinesq equations will have to concentrate on modification of the convective kernels to involve buoyancy forces in a natural way, rather than as pseudo-body forces. The integral formulation proposed in this paper could be easily extended to three-dimensional problems, however the main challenge in implementation is associated with the mesh. In particular, the commonly used three-dimensional polyhedra are not acceptable for maintaining proper inter-region compatibility.

Acknowledgements

References

[1] C. Baiocchi, F. Brezzi, L.P. Franca, Virtual bubbles and the Galerkin-least-squared method, Comput. Meth. Appl. Mech. Engrg. 105 (1993) 125–141.

[2] P.K. Banerjee, K.A. Honkala, Development of BEM for thermoviscous flow, Comput. Meth. Appl. Mech. Engrg. 151 (1998) 43–61.

[3] A. Brooks, T.J.R. Hughes, Streamline upwind/Petrov–Galerkin formulation for convection dominated flow with particular emphasis on the incompressible Navier–Stokes equations, Comput. Meth. Appl. Mech. Engrg. 30 (1982) 199–259.

[4] M.B. Bush, Modelling two-dimensional flow past arbitrary cylindrical bodies using boundary element formulations, Appl. Math. Modelling 7 (1983) 386–394.

[5] S. Chandrasekhar, Hydrodynamic and Hydromagnetic Stability, Oxford University Press, Oxford, 1980.

[6] V. Dakshina Murty, A numerical investigation of Benard convection using finite elements, Computers & Fluids 14 (1986) 379–391.

[7] G.F. Dargush, P.K. Banerjee, A boundary element method for steady incompressible thermoviscous flow, Internat. J. Numer. Meth. Engrg. 31 (1991) 1605–1626.

[8] G.F. Dargush, P.K. Banerjee, Y. Shi, Development of an integrated BEM approach for hot fluid structure interaction, NASA CR-187236, NASA Lewis Research Center, Cleveland, Ohio, 1991.

[9] G. De Vahl Davis, I.P. Jones, Natural convection in a square cavity: a comparison exercise, Internat. J. Numer. Meth. Fluids 3 (1983) 227–248.

[10] G. De Vahl Davis, Natural convection of air in a square cavity: a bench mark numerical solution, Internat. J. Numer. Meth. Fluids 3 (1983) 249–264.

[11] L.P. Franca, S.L. Frey, T.J.R. Hughes, Stabilized finite element methods: I. Application to the advective–diffusive model, Comput. Meth. Appl. Mech. Engrg. 95 (1992) 253–276.

[12] L.P. Franca, S.L. Frey, Stabilized finite element methods: II. The incompressible Navier–Stokes equations, Comput. Meth. Appl. Mech. Engrg. 99 (1992) 209–233.

[13] D.K. Gartling, A test problem for outflow boundary conditions – flow over a backward-facing step, Internat. J. Numer. Meth. Fluids 11 (1990) 953–967.

[14] M.M. Grigor'ev, A boundary element method for the solution of convective diffusion and Burgers' equations, Internat. J. Numer. Meth. Heat & Fluid Flow 4 (1994) 527–552.

[15] M.M. Grigoriev, A.V. Fafurin, A boundary element method for steady viscous flow using penalty function formulation, Internat. J. Numer. Meth. Fluids 25 (1997) 907–929.

[16] M.M. Grigoriev, G.F. Dargush, A poly-region boundary element method for incompressible viscous fluid flows, Internat. J. Numer. Meth. Engrg. 46 (1999) 1127–1158.

[17] M. Hribersek, L. Skerget, Fast boundary-domain integral algorithm for the computation of incompressible fluid flow problems, Internat. J. Numer. Meth. Fluids 31 (1999) 891–907.

[18] T.J.R. Hughes, Simple finite element scheme for developing upwind finite elements, Internat. J. Numer. Meth. Engrg. 12 (1978) 1359–1365.

[19] T.J.R. Hughes, A. Brooks, Multi-dimensional upwind scheme with no crosswind diffusion, AMD, v 34, in: T.J.R. Hughes (Ed.), Finite Element Methods for Convection Dominated Flows, Symp. Winter Ann. Meeting of ASME, New York, 1979, pp. 19–35.

[20] T.J.R. Hughes, Multiscale phenomena: Green's functions, the Dirichlet-to-Neumann formulation, subgrid scale models, bubbles and the origins of stabilized methods, Comput. Meth. Appl. Mech. Engrg. 127 (1995) 387–401.

[21] T.J.R. Hughes, J.R. Stewart, A space-time formulation for multiscale phenomena, J. Comput. Appl. Math. 74 (1996) 217–229.

[22] M. Kanoh, G. Aramaki, T. Kuroki, Stability experiment of FDM, FEM and BEM in convective diffusion, in: C.A. Brebbia, G. Maier (Eds.), Boundary Elements VIII, Springer, Berlin, 1986, pp. 725–733.

[23] K. Kitagawa, Boundary element analysis of viscous flow, in: Lecture Notes in Engineering, Springer, Berlin, 1990.

[24] S.H. Lee, L.G. Leal, Low-Reynolds-number flow past cylindrical bodies of arbitrary cross-sectional shape, J. Fluid Mech. 164 (1986) 401–427.

[25] J.M. Leone Jr., Open boundary condition Symposium benchmark solution: stratified flow over a backward-facing step, Internat. J. Numer. Meth. Fluids 11 (1990) 969–984.

[26] N. Okamoto, Analysis of convective diffusion problem with first-order chemical reaction by boundary element method, Internat. J. Numer. Meth. Fluids 8 (1988) 55–64.

[27] C.W. Oseen, Neuere Methoden und Ergebnisse in der Hydrodynamik, Akademische Verlagsgesellschaft, Leipzig, 1927.

[28] O. Østerby, Z. Zlatev, Direct methods for sparse matrices, in: Lecture Notes in Computer Science, vol. 157, Springer, Berlin, 1983, pp. 1–119.

[29] M. Ramsak, L. Skerget, Mixed boundary elements for laminar flows, Internat. J. Numer. Meth. Fluids 31 (1999) 861–877.

[30] Y. Shi, P.K. Banerjee, Boundary element methods for convective heat transfer, Comput. Meth. Appl. Mech. Engrg. 105 (1993) 261–284.

[31] L. Skerget, N. Samec, BEM for non-Newtonian fluid flow, Engineering Analysis with Boundary Elements 23 (1999) 435–442.

[32] P. Skerget, I. Zagar, A. Alujevic, Three-dimensional steady-state diffusion–convection, in: C.A. Brebbia, W.L. Wendland, G. Kuhn (Eds.), Boundary Elements IX, vol. 3, Springer, Berlin, 1987, pp. 303–312.

[33] Y. Tanaka, T. Honma, I. Kaji, Boundary element solution of a three-dimensional convective diffusion equation for large Peclet numbers, in: M. Tanaka, T.A. Cruse (Eds.), Boundary Element Meth. Appl. Mech., Pergamon, Oxford, 1988, pp. 295–304.

[34] G.K. Youngren, A. Acrivos, Stokes flow past a particle of arbitrary shape: a numerical method of solution, J. Fluid Mech. 69 (1975) 377–403.